

Journal of
Applied Remote Sensing

RemoteSensing.SPIEDigitalLibrary.org

Estimation of surface latent heat fluxes in an oasis utilizing a two-source energy balance model based on land surface temperature decomposition

Runke Wang
Jian Wang
Gaofeng Zhu
Hongyi Li
Donghang Shao
Xiaohua Hao

SPIE.

Runke Wang, Jian Wang, Gaofeng Zhu, Hongyi Li, Donghang Shao, Xiaohua Hao, "Estimation of surface latent heat fluxes in an oasis utilizing a two-source energy balance model based on land surface temperature decomposition," *J. Appl. Remote Sens.* **13**(3), 034504 (2019), doi: 10.1117/1.JRS.13.034504.

Estimation of surface latent heat fluxes in an oasis utilizing a two-source energy balance model based on land surface temperature decomposition

Runke Wang,^{a,b} Jian Wang,^{a,*} Gaofeng Zhu,^c Hongyi Li,^a Donghang Shao,^d and Xiaohua Hao^a

^aChinese Academy of Sciences, Northwest Institute of Eco-Environment and Resources, Heihe Remote Sensing Experimental Research Station, Key Laboratory of Remote Sensing of Gansu Province, Lanzhou, China

^bUniversity of Chinese Academy of Sciences, Beijing, China

^cLanzhou University, Key Laboratory of Western China's Environmental Systems (Ministry of Education), Lanzhou, China

^dUniversity of Electronic Science and Technology of China, School of Resources and Environment, Chengdu, Sichuan Province, China

Abstract. Latent heat flux is the main indicator of regional water-heat balance and plays an important role in drought monitoring and water resource management. Here, we attempt to estimate latent heat flux using a two-source energy balance model (TSEB). The decomposition algorithm of soil surface temperature and vegetation canopy temperature is discussed, and it is a key factor for calculating the latent heat flux in the TSEB model. Temperature decomposition was conducted using two methods: one is based on a simple linear relationship between the canopy temperature and directional radiation temperature and the other is based on soil latent heat flux expressed by the Priestley–Taylor formula. Then, the soil temperature was estimated using the soil latent heat flux. The estimation of the surface heat flux was based on the soil and vegetation canopy temperatures. The results show that the Priestley–Taylor formula method provided more accurate estimates of the latent heat flux than the linear relation method, and the reliability and precision were improved. The root-mean-squares error of the former method decreased by 38.8% compared with the latter method. The TSEB model was used to estimate the surface heat flux, and it was feasible for monitoring drought in typical drought-prone regions. © 2019 Society of Photo-Optical Instrumentation Engineers (SPIE) [DOI: 10.1117/1.JRS.13.034504]

Keywords: remote sensing; surface energy balance; component temperatures; latent heat flux.

Paper 180848 received Oct. 30, 2018; accepted for publication Jun. 25, 2019; published online Jul. 16, 2019.

1 Introduction

Latent heat flux (λE) and its components, soil and canopy latent heat fluxes, are essential to the land hydrologic cycle and reflect the quality and energy exchange between the ecosystem and the atmosphere.¹ In agriculture, the accurate estimation of λE and its components is essential for agricultural irrigation systems and crop harvest predictions.² If the canopy latent heat flux can be reduced by changing the microclimate of the crop canopy, then the latent heat flux can contribute to the production of crops indirectly.³

Thus far, many methods have been proposed to estimate λE from ground-based point observations or estimation methods.^{4–7} However, the available observations are not sufficient to reveal continuous, large-scale variations in λE . Some methods have been proposed to estimate λE from remote sensing observations at the regional scale. The main methods for estimating λE include the one-source model (OSM)^{8–10} and two-source energy balance model (TSEB).¹¹ The OSM assumes that the land surface is homogeneous and does not distinguish between soil and vegetation. This model assumes that the energy exchange interface is a large leaf and that latent heat

*Address all correspondence to Jian Wang, E-mail: wjian@lzb.ac.cn

exchange occurs on the leaf surface. However, such a hypothesis is not applicable to sparsely covered areas, especially in arid and semiarid areas. To overcome the limitation of the OSM, the TSEB model was first proposed in 1995 (called the N95 model) by Kustas et al.¹² and Zhan et al.¹³ as a more realistic description of turbulence and radiation exchange over a partial vegetation canopy.¹⁴ Therefore, the TSEB model has become the main method to estimate the land surface sensible heat flux (H) and λE .^{15–19} The TSEB model partitions the underlying surface into independent sources of soil and vegetation and transmits the sensible and latent heat fluxes into the atmosphere. The heat flux from the soil surface is assumed to be parallel to the heat flux from the canopy leaves.¹¹ The parallel agreement may be slightly more appropriate for sparser, clumped vegetation in a semiarid region because the soil surface interacts less with a sparse vegetation canopy than a dense vegetation canopy. This partition is reasonable for natural semiarid ecosystems or deficit-irrigated crops in arid and semiarid regions where water is limited over a wide range of regions.²⁰ The TSEB model is mainly used to improve the estimation accuracy of latent heat fluxes in partial vegetation cover regions.^{11,21–23} Previous studies have found that the TSEB model is advantageous over the OSM, especially for sparse surfaces.¹¹ In the TSEB model, the soil and canopy latent heat fluxes are obtained based on the energy balance equation.²⁴ Finally, the latent heat flux (soil plus canopy latent heat flux) is obtained.

The directional radiometric temperature (T_R) is a very important factor for estimating land surface heat fluxes. In the estimation of land surface fluxes, there are a wide range of operational remote sensing models depending on the use of T_R .²⁵ In the TSEB model, T_R is expressed as a composite of the vegetation canopy (T_c) and soil surface (T_s) temperatures.¹¹ When the values of T_c and T_s are obtained, the net radiation and surface fluxes can be estimated using the TSEB model. Hence, the component temperature decomposition is the most important and key problem for estimating surface heat fluxes. An initial estimation of T_c is made assuming non-water-stressed conditions, and T_c is estimated by applying the Priestley–Taylor formula,²⁶ which was proposed by Norman et al.¹¹ There are two methods for estimating T_s . First, T_s is obtained via a linear relation among T_c , T_R , and T_s (termed the TSEB- T_R method). This method is applied in the initial TSEB model,¹¹ and vegetation coverage is used as an input parameter in this method. Second, obtaining T_s first involves using the Priestley–Taylor formula to estimate the soil surface latent flux;²⁷ then, the energy balance equation is used to calculate T_s (termed the TSEB-PT method). It is necessary to determine which of these two methods is more appropriate for calculating soil surface temperature in arid and semiarid regions. The best method can be determined by comparing the two methods. The appropriate T_s parameterization method is of great significance for improving the accuracy of heat flux estimation in arid areas.

In this paper, we report on estimates of surface latent heat fluxes in an oasis utilizing a TSEB model based on land surface temperature (LST) decomposition. The main objectives were as follows: (i) we apply two different methods to decompose the LST into T_c and T_s ; (ii) based on the component temperature decomposition results, the heat flux is estimated and compared with the observed data; and (iii) the available energy and turbulent energy fluxes are compared between the two methods to reveal the energy balance problem.

2 Materials and Methods

2.1 Study Area

For this study, the middle reaches of the Heihe River basin were selected. The elevation is ~1550 m. The scope of the study area is 30 km × 30 km, including a kernel research region of ~5 × 5 km, located in the middle of the Hexi Corridor, Gansu Province, China (Fig. 1). Less precipitation occurs in this area, which is a typical, temperate, dry continental climate, and evaporation is very large. From 1960 to 2000, the average annual temperature and precipitation were 7.2°C and 126.7 mm,²⁸ respectively. The vegetation is seasonal, and plants grow sparsely in natural environments. In oasis areas, the agriculture is irrigated. July and August are the peak seasons for vegetation growth.

The underlying surfaces in the research area are cropland, sandy desert, desert steppe, the Gobi Desert, wetland, and residential areas (Fig. 2). Vegetation is rare in the natural environment, and the

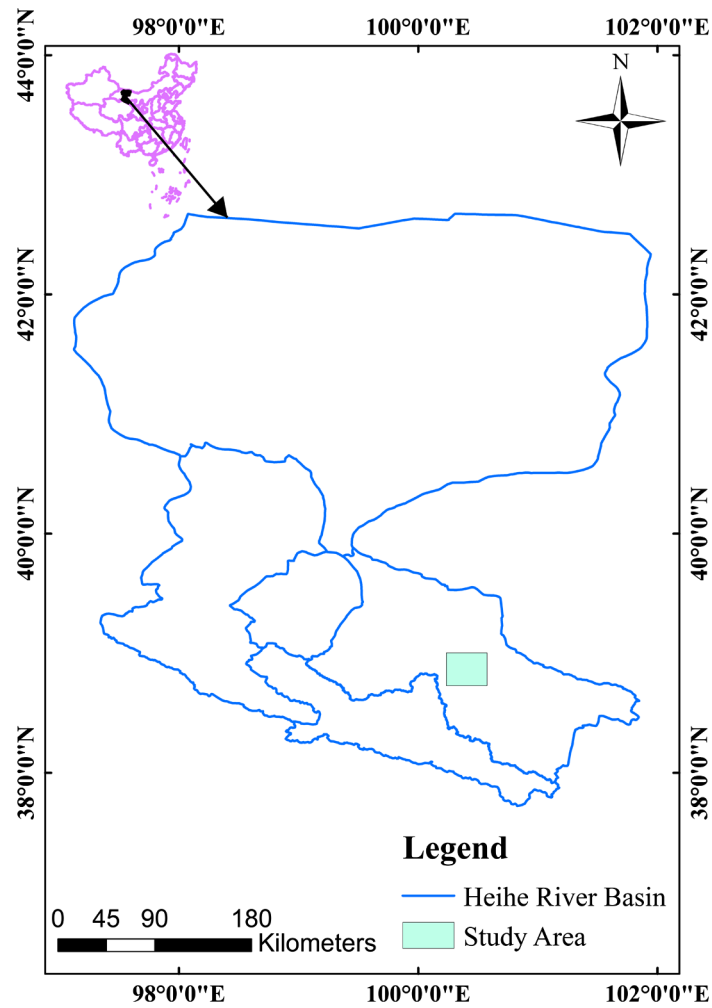


Fig. 1 Location of the study area in the middle reaches of the Heihe River basin, Gansu, China.

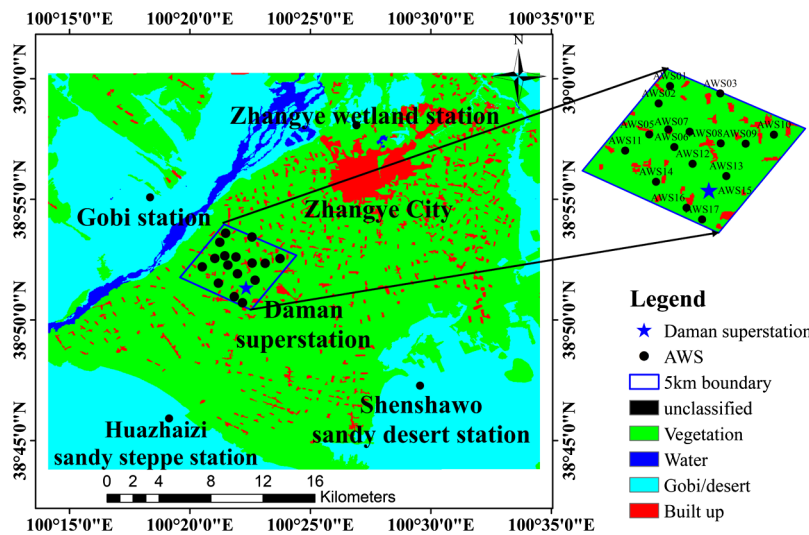


Fig. 2 Spatial distribution of the AWS sites and land use classifications used in this study.

main vegetation on the surface is crop plants. The main irrigated agriculture is maize; in this study, the maize was seeded in April, the planting density was $10.6 \text{ seeds m}^{-2}$, the row spacing was 43 cm, and the plant spacing was 22 cm. The maize crops used a water-saving drip irrigation system. There was no significant difference in the spatial heterogeneity at pixel scales.

2.2 Remote Sensing Data

The satellite data were obtained from advanced spaceborne thermal emission and reflection radiometer (ASTER) satellite images. The ASTER sensor provides 14 bands of spectral information, including visible and near-infrared, shortwave infrared (SWIR), and thermal infrared (TIR). ASTER has five thermal wave bands ranging from 8 to $12 \mu\text{m}$, with a spatial resolution of 90 m, which is resampled to 30 m. In this study, we selected nine clear-sky ASTER images, and the day of year (DOY) values were from June to September 2012 (DOY 167, 176, 192, 215, 224, 231, 240, 247, and 256).

The LST and emissivity (LSE) information were derived from ASTER data using the TES algorithm²⁹ combined with the water vapor scaling (WVS) atmospheric correction method.³⁰ In this paper, the downloaded ASTER LST and LSE dataset in 2012 in the middle reaches of the Heihe River Basin was used as the estimation values of surface temperature.³¹ The accuracy of the LST retrieved with the TES algorithm is within 1.5 K of the absolute value, and the accuracy of the emissivity is within 0.015 of the absolute value.^{29,32}

2.3 Observational Data

The ground observation data came from the Heihe Watershed Allied Telemetry Experimental Research (HiWATER) dataset. The overall objective of HiWATER was to enhance the applicability of remote sensing in integrated ecohydrological studies and water resource management at the basin scale.³³ The HiWATER experiment has a good research foundation and abundant data accumulation.³³ The data are open, shared, and can be downloaded for free.³⁴ The observational data include automatic weather station (AWS) and eddy covariance (EC) data. The spatial distribution of the observation sites is shown in Fig. 2.

The observational data spanned the period from May to September 2012, and 17 EC observations in this region were used. The sonic anemometers of the ECs were installed at heights of ~ 2.81 and 3.15 m except for one EC with a height of 34 m in the upper layer of the Daman superstation. Five EC combinations were used in the matrices, namely, CSAT3 and Li7500 [sites 2, 5, 8, 10, 11, 12, 14, and the Batman Gobi site (GB), Shenshawo desert site (SSW), and Huazhaizi desert steppe site (HZZ)], CSAT3 and Li7500A (sites 4, 6, 7, 13, and 15), CSAT3 and EC150 (site 17), Gill and Li7500 (site 16), and Gill and Li7500A (sites 1, 3, 9, and the Zhangye wetland site).²⁸ The sampling frequency of the EC instrument was 10 Hz, and the average value over 30 min was recorded. The data record was based on Beijing time.

The AWS observation matrix in the middle reaches of the Heihe River basin contained 21 sites (Fig. 2). The site locations included a vegetable field (AWS 01), maize fields (AWS 02, 03, 05 to 13), village (AWS04), orchard (AWS17), GB (AWS 18), SSW (AWS 19), HZZ (AWS 20), and wetland (AWS 21). The AWSs included the following instruments: HMP45C (Vaisala, Inc., Finland), 010C-1/020C-1 (Metone, Inc.), Kipp and Zonen CM3 (Campbell Scientific Ltd.), HFP01 (Campbell Scientific Ltd.), and Campbell 109 (Campbell Scientific Ltd.).²⁸

Soil temperature probes (Campbell 109) were placed on the ground and buried at depths of 2, 4, 10, 20, 40, 80, 120, and 160 cm below the ground to ensure 144 data points per day (every 10 min). In this paper, the surface temperature of the soil at 0 cm was used. Time was consistent with the overpass times of the ASTER satellite.

2.4 Data Processing

2.4.1 Footprint model

The footprint is also called the source weight function. The area that contributes most to the flux observations is called the flux contribution area or source area.³⁵ The purpose of the flux

observation footprint and source area is to solve the problem of point-to-surface or line-to-surface spatial representation, which should not be ignored in flux observations. The range of flux sources can be used to evaluate the spatial representativeness of flux data quantitatively.³⁶ The characteristics of the EC footprint area were analyzed in other regions,³⁷ and then the flux source area model of Schmid³⁸ was applied to obtain the flux footprint of a single point. However, Liu et al.²⁸ applied the Euler analytical flux footprint model to obtain the flux footprint of single-point vertical flux measurements³⁹ and considered the flux contribution of the chosen total source area to be 80%.

2.4.2 LAI measured

LAI measurements were collected using an LAI-2000 plant canopy analyzer (PCA, Li-Cor, Lincoln, Nebraska). The collection time was concentrated between 07:00 and 10:00 a.m. to avoid errors caused by direct sunlight. During data acquisition, eight points were uniformly selected in each sample location and the 30 × 30 m surrounding area, and nine LAI data points were obtained; then, the average value was calculated to represent the sample area.

2.4.3 LST estimate

LST was estimated from the upwelling and downwelling longwave radiation data observed on the ground as follows:⁴⁰

$$\text{LST} = [(R_{lw}^{\uparrow} - (1 - \varepsilon)R_{lw}^{\downarrow})/(\varepsilon\sigma)]^{1/4}, \quad (1)$$

where R_{lw}^{\downarrow} is the longwave radiation from the sky; R_{lw}^{\uparrow} is the longwave radiation from the land surface; ε is the emissivity of the surface broadband radiation, which was assigned an empirical value of 0.985; and σ is the Stefan–Boltzmann’s constant ($5.67 \times 10^{-8} \text{ Wm}^{-2} \text{ K}^{-4}$). In this paper, the value of the LST’s surface estimation was approximately regarded as the observed LST.

2.5 TSEB Model

In the TSEB model, the latent heat flux (λE) was partitioned into vegetation canopy (λE_c) and soil surface (λE_s) components fluxes, and λE_c and λE_s are expressed as the remainders of the soil and vegetation energy balance:

$$\lambda E_c = R_{nc} - H_c, \quad (2)$$

$$\lambda E_s = R_{ns} - H_s - G, \quad (3)$$

where H_c and H_s are the sensible heat fluxes of the vegetation canopy and soil surface, respectively, G is the soil heat flux, and R_{ns} and R_{nc} are the soil surface and vegetation canopy net radiation, respectively. The values of R_{ns} and R_{nc} are estimated using longwave and shortwave radiation.¹⁵

G is estimated using the model given by Santanello and Friedl,⁴¹ where G is a function of R_{ns} and expressed as follows:

$$G = a \cos[2\pi(t + c)/b]R_{ns} \quad R_{ns} > 0, \quad (4)$$

where t is the solar time angle (s) and a , b , and c are empirical constants ($a = 0.30$, $b = 86,400 \text{ s}$, and $c = 3600 \text{ s}$ ^{20,42}).

H is estimated using the temperature gradient-transport and resistance networks. The sensible heat flux for the vegetation canopy and soil surface were considered to be parallel to each other.¹¹ Therefore, the sensible heat fluxes from the soil and vegetation and the sensible flux of soil plus vegetation can be expressed as follows:

$$H_c = \rho C_p \frac{T_c - T_a}{R_a}, \quad (5)$$

$$H_s = \rho C_p \frac{T_s - T_a}{R_s + R_a}, \quad (6)$$

$$H = \rho C_p \left(\frac{T_c - T_a}{R_a} + \frac{T_s - T_a}{R_a + R_s} \right), \quad (7)$$

where ρ is the air density (kg m^{-3}), T_a is the air temperature at the reference height (K); C_p is the volumetric heat capacity of air (assumed to be a constant at $1013 \text{ Jkg}^{-1} \text{ K}^{-1}$); R_s is the resistance to heat flow in the boundary layer immediately above the soil surface (s m^{-1}), which was estimated according to Kustas et al.;⁴³ and R_a is the aerodynamic resistance (s m^{-1}), and the value of R_a in the surface layer was estimated according to Brutsaert.⁴⁴

The values of H_c and H_s were determined using Eqs. (5) and (6), where the calculations of the parameters T_c and T_s are very important, as the accuracies of T_c and T_s affect the sensible heat flux results. In fact, even with portable infrared thermometers being used in a small-scale region, T_c and T_s are difficult to obtain.⁴⁵ Therefore, the decomposition of T_c and T_s from the LST retrieval was determined to be an effective method.

2.6 Component Temperature Decomposition

2.6.1 TSEB- T_R method

The Priestley–Taylor formula, which was proposed by Norman et al.¹¹ and supported by Kustas and Anderson²⁵ and Agam et al.,²⁷ was applied to estimate T_c .²⁶

$$T_c = T_a + \frac{R_{nc} R_a}{\rho C_p} \left(1 - \alpha_c f_g \frac{\Delta}{\Delta + \gamma} \right), \quad (8)$$

where α_c is the Priestley–Taylor parameter for the canopy, Δ is the slope of the saturation vapor pressure versus temperature curve (kPa K^{-1}), γ is the psychrometric constant (0.066 kPa K^{-1}), and f_g is the fraction of the leaf area index that is green. The value of f_g can be estimated using remote sensing data.^{46,47} Initial estimates of R_{nc} were estimated in the original form of the TSEB model¹¹ and expressed as follows:

$$R_{nc} = R_n [1 - \exp(-\beta \text{LAI})], \quad (9)$$

$$\text{LAI} = -2 \cos(\theta) \ln(1 - f_c), \quad (10)$$

where β is the extinction coefficient, ($\beta \approx 0.95^{15}$), LAI is the leaf area index, f_c is the vegetation cover fraction, and θ is the zenith angle.

In the TSEB- T_R method, the LST retrieval from the TIR remote sensing data is regarded as T_R rather than the aerodynamic temperature in the TSEB model.¹¹ T_R is obtained as a weighted composite of T_c and T_s . The T_s value was estimated based on f_c . This method was proposed by Norman et al.,¹¹ and the expression is as follows:

$$T_s = \left[\frac{\varepsilon T_R^4 - \varepsilon_c f_c T_c^4}{\varepsilon_s (1 - f_c)} \right]^{1/4}, \quad (11)$$

$$\varepsilon = \varepsilon_c f_c + \varepsilon_s (1 - f_c) + d\varepsilon, \quad (12)$$

$$f_c = \frac{\text{NDVI} - \text{NDVI}_s}{\text{NDVI}_v - \text{NDVI}_s}, \quad (13)$$

where NDVI is the normalized differential vegetation index, NDVI_s represents the NDVI in areas completely covered by bare soil or vegetation-free areas, and NDVI_v represents the

NDVI in areas completely covered by vegetation. Here, ε_c and ε_s are the emissivities of full vegetation and bare soil, respectively, and the values of ε_c and ε_s in this paper are 0.98 and 0.95, respectively. The emissivity of a heterogeneous surface is expressed in previous studies.^{48,49} Note that $d\varepsilon$ is the multiple scattering contribution caused by the internal combination of a pixel and emissivity.

2.6.2 TSEB-PT method

Agam et al.²⁷ developed a conceptual relation between α_{bulk} (bulk α)⁵⁰ and both α_s and α_c . For this reason, the estimation of λE_s can be estimated using Priestley–Taylor equation. However, under the condition of high vegetation coverage and advection, α_c is difficult to adjust, which may lead to an overestimation of λE_s .⁵¹ On this basis, Song et al.⁴² proposed to estimate λE_s based on the TSEB-A model. The method added soil water stress factors controlled by soil water to estimate λE_s under dry surface conditions. In agricultural experiments, the TSEB-A method is more likely to produce smaller errors in estimating T_s , T_c , and λE , especially in the case of higher vegetation coverage.⁴²

Based on the TSEB-A model, λE_s is expressed as follows:

$$\lambda E_s = f_{sw} \alpha_s \frac{\Delta}{\Delta + \gamma} (R_{ns} - G), \quad (14)$$

where f_{sw} is the soil water stress, which is used to adjust soil evaporation under drier surface conditions.⁴² The value of f_{sw} can be estimated using the surface the soil water content (0 to 10 cm).⁵² α_s is the Priestley–Taylor parameter applied to the soil. R_{ns} can be estimated using the exponential extinction of the net radiation;¹⁵ however, this method can result in an error of over 50 Wm^{-2} . Hence, in this study, R_{ns} is estimated using longwave and shortwave net soil radiation.¹⁵ T_s is solved by combining Eqs. (6) and (14):

$$T_s = T_a + \frac{(R_a + R_s)}{\rho c_p} \left[\left(1 - f_{sw} \alpha_s \frac{\Delta}{\Delta + \gamma} \right) (R_{ns} - G) \right], \quad (15)$$

where α_s and α_c are given by Agam et al.;²⁷ the other terms were previously defined in this paper.

In the TSEB-PT method, the value of T_c is estimated using Eq. (8), and T_s is estimated using Eq. (15). However, T_c and T_s are estimated using the soil and vegetation net radiation formulas,^{15,42} respectively. In this case, T_c and T_s are solved using a secant method. Determining the soil moisture is a key problem. The water content of the observation site in the study area is observed by a reflectometer at the depth of 0 to 10 cm, and the average value is estimated.

2.7 Validation of the Estimation Results

Based on the geolocation information (latitude and longitude) of each site, the estimated values were extracted for the pixel closest to the observation site. Next, the estimated values were matched with the ground observation according to the satellite observation time. If the observation values were missing, the corresponding remote sensing images were removed. In addition, all valid points were also manually examined to exclude cloud-contaminated pixels with unreasonable values.

For model evaluation, surface energy fluxes (R_n , λE , H , and G) from the flux datasets (observed values) were compared to model outputs (estimated values) using different methods.⁵³ These methods include the root-mean-squares error (RMSE), mean absolute error (MAE), and Pearson correlation coefficient (R). For the calculation formulas of R , RMSE, and MAE, refer to Norman et al.¹¹ R was used to indicate the degree of correlation between estimated and observed surface energy fluxes; the RMSE was used to measure differences in accuracy between the model-estimated values and observations from the flux towers; the MAE was used to indicate the magnitude of the average absolute difference in the observed and estimated values; and finally, the mean absolute percentage error (MAPE) was used to express the magnitude of the

absolute difference between the observed and estimated values relative to the observed average value.

3 Results

3.1 LAI

The LAI was estimated based on NDVI using Eqs. (10) and (13). The estimated values of LAI range widely from 0.524 to 3.89. The estimated LAI values are compared with the average values of multiple observations at adjacent locations of observation stations. In the LAI remote sensing image, the pixels corresponding to the geographic coordinates of the ground observation points are found out. The pixel values were used as the estimated LAI values. Then, the LAI estimation was validated based on the ground observation values. The estimated LAI validation only considered the corresponding pixels at the observation site.

Based on the simulation results (Fig. 3), in the early stage of crop growth (from DOY 151 to DOY 176), the estimated LAI is less than the field measurement value, with a relative error of $\sim 12.8\%$. The period up to DOY 192 corresponds to the maximum LAI. Moreover, the estimated LAI value is 3.89, and the observed LAI value is 4.02. These values correspond to the middle of crop growth (from DOY 176 to DOY 240), and there is little difference between the estimated and observed values. At the later stage of crop growth (from DOY 240 to DOY 256), the LAI decreases gradually as the leaves begin to senesce. The observed LAI value in the late stage of crop growth is greater than that of the estimated value [Fig. 3(a)]. The largest difference occurs on DOY 256, when the leaves are gradually dried up. Over the entire season of crop growth, the estimated values are consistent with the observed values in time and space.

According to the scatter plots of the LAI using the estimated and observed values [Fig. 3(b)], the correlation between them is quite good ($R = 0.94$); the RMSE and MAE are 0.44 and 0.33, respectively. The estimated LAI is generally below the 1:1 line, indicating that it is below the observed value.

3.2 Verification of the Estimated LST

The estimated LST values were compared with the LST values derived from land surface estimation based on Eq. (1). The results show that the estimated LST values are highly accurate, therefore the result is reasonable (Fig. 4). The estimated values are quite similar to the observed values over a reasonable range ($290 \text{ K} < \text{LST} < 325 \text{ K}$), and the time distribution trend is similar to that of the air temperature (air temperature data not shown). R is 0.96, reflecting a strong correlation between the estimated and observed values. The MAE and RMSE are 1.37 and 1.6 K, respectively. Both values are less than 2 K. The MAE in this study fits well with the results by Gillespie et al.,²⁹ where the MAE was within 1.5 K. The 1:1 line shows good conformity between the estimated and observed values. The slope of the linear regression equation

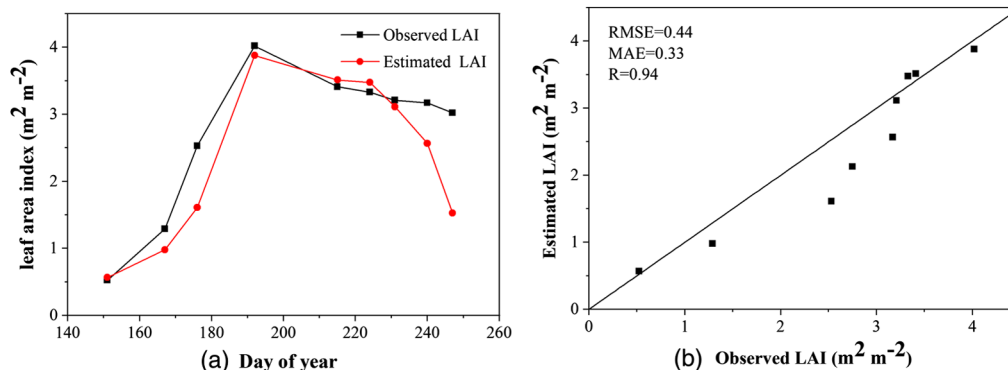


Fig. 3 Estimated LAI values compared with the observed LAI values during the crop growing season.

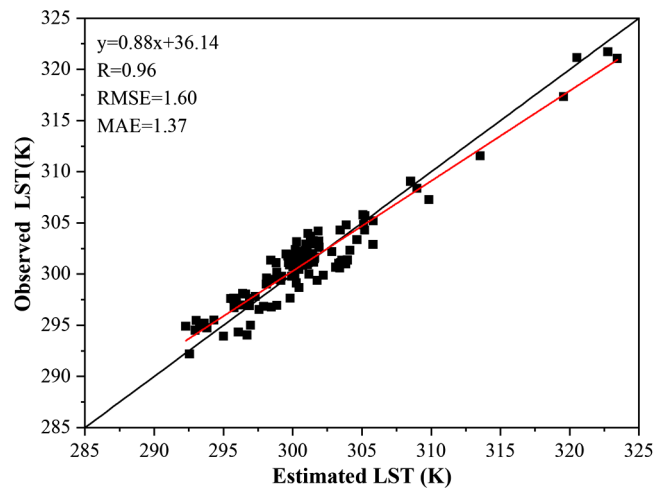


Fig. 4 Comparison of the estimated and observed LSTs in the study area; the LST values were retrieved from ASTER data. The line represents a 1:1 relationship.

between the estimated and observed values is 0.88, and the fitting degree between these values is better.

3.3 Estimated versus Observed Soil Surface Temperatures

The vegetation temperature difference obtained by the two methods is not obvious in the spatial distribution, and the canopy temperature is relatively uniform (figure not shown). The images show the results of T_s using the TSEB-PT method (Fig. 5). Considering that the LAI values of deserts, the Gobi, and water bodies are very small, the LST of the previously retrieved desert, Gobi, and water body areas can be approximated as T_s . Therefore, the Gobi, desert, wetland, water body, and residential areas are masked by the land cover types, and T_s in oasis areas is estimated. Affected by the shadows of trees and buildings, T_s is lower around towns and villages and higher near desert and Gobi farmland. Overall, T_s does not change significantly in space.

The difference in T_s estimated by the TSEB-PT and TSEB- T_R methods is shown in Fig. 6. Significant differences in T_s are found between the two results. The T_s difference is shown in Figs. 6(a) to 6(d) and 6(g), ranging from 5 to 10 K, and Figs. 6(e), 6(f), 6(h), and 6(i) have a T_s difference of more than 10 K. The spatial variation shows that the difference between T_s estimated using the two methods is large. This tendency indicates that one of the two methods for calculating T_s may overestimate T_s . Therefore, it is very important to choose the appropriate decomposition method for improving the accuracy of surface heat flux estimation.

The time consistency between the observed and estimated values of the average T_s in arid and semiarid oasis areas is shown in Fig. 7(a). During the early season when the LAI does not reach its maximum value, the surface vegetation is partly covered and the vegetation and soil are distinct. In this case, there are significant differences between the estimated and observed average temperatures and the estimated values are overestimated. During the mid-season period (from DOY 176 to 240) when the LAI reaches a maximum, f_c is close to 1.0, the leaves intercept the sunlight before reaching the surface, and the observation of the average T_s is affected by vegetation canopy shadows. At this time, T_s obtained by the two methods is larger than the observed T_s , except DOY 176, the average estimated value by the TSEB-PT method is slightly lower than the average observed value. During the end of crop growth, the average T_s estimated with the TSEB-PT method is close to the observed value, but the average T_s estimated using the TSEB- T_R method is larger than the observed value [Fig. 7(a)]. The MAEs between the TSEB-PT and TSEB- T_R methods are compared in Fig. 7(b). The TSEB- T_R method resulted in an MAE value greater than that obtained using the TSEB-PT method except for DOY 240. Using the TSEB- T_R method, the maximum MAE appears on DOY 231, which is 7.25 K. The maximum MAE is 2.76 K for the TSEB-PT method, which appears on DOY 240. The minimum MAE values appear on DOY 224, which are 0.86 and 1.65 K, respectively.

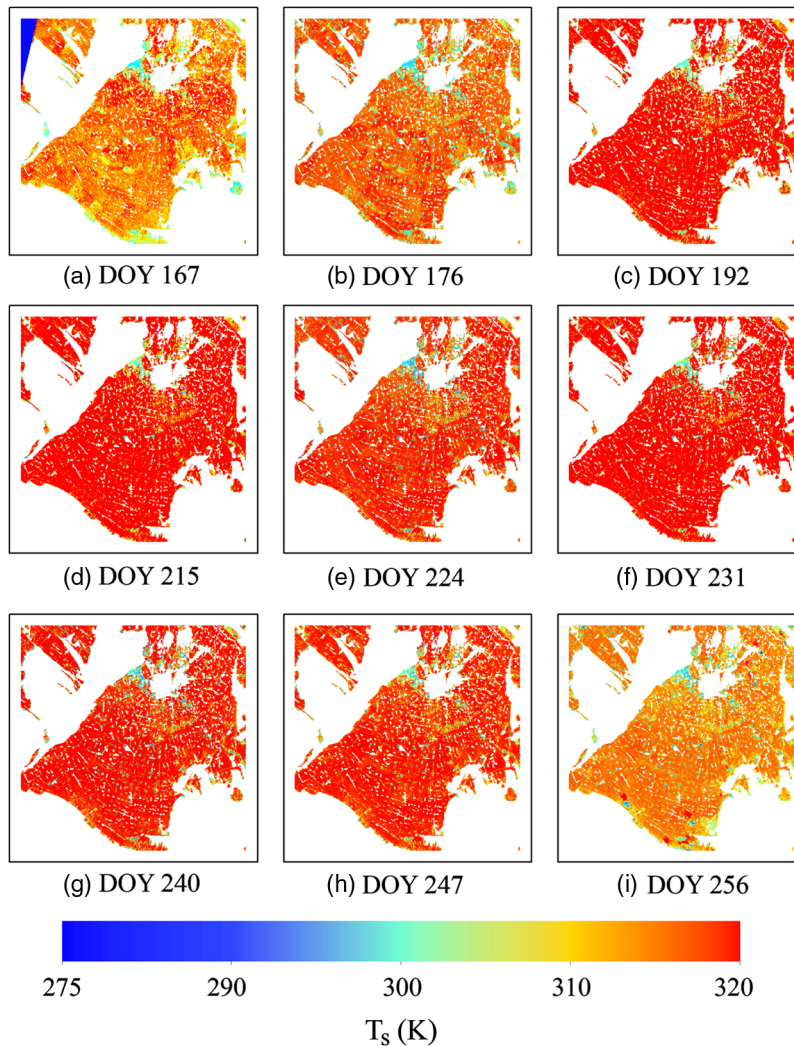


Fig. 5 Soil temperature images from the component temperature decomposition using the TSEB-PT method. The oasis area excludes Gobi, desert, wetland, water body, and residential areas.

The estimated and observed values of T_s obtained using the TSEB-PT method are consistent; the R value is 0.92, and the RMSE and MAE are 2.32 and 2.01 K, respectively [Fig. 8(a)]. However, T_s derived from the TSEB- T_R method has R , RMSE, and MAE values of 0.88, 5.04, and 4.01 K, respectively [Fig. 8(b)]. The discrepancy between the TSEB- T_R and TSEB-PT methods is indicated by differences in the RMSE and MAE. The RMSE and MAE results obtained using the TSEB-PT method are relatively small compared to those obtained using the TSEB- T_R method. RMSE% and MAE% as a percentage of the observed T_s average are 0.78% and 0.67% by use of the TSEB-PT method, and 1.69% and 1.3% by use of the TSEB- T_R method. The error span is large; hence, the TSEB- T_R method may be limited when estimating T_s . The estimated values of the two methods are overestimated compared with the observed values. The results show that when using the TSEB-PT method, the data points are more concentrated. In contrast, the results from the TSEB- T_R method are more scattered.

3.4 Land Surface Heat Fluxes Estimated with the TSEB Model

The average R_n and G values were estimated for selected days. These values reflect the changing trend over time and the discrepancy between the estimated and observed values. The results show that the average R_n ranges from 500 to 700 W m^{-2} [Fig. 9(a)]. The observed R_n values obtained by the use of the TSEB-PT method are underestimated, especially in the middle and late

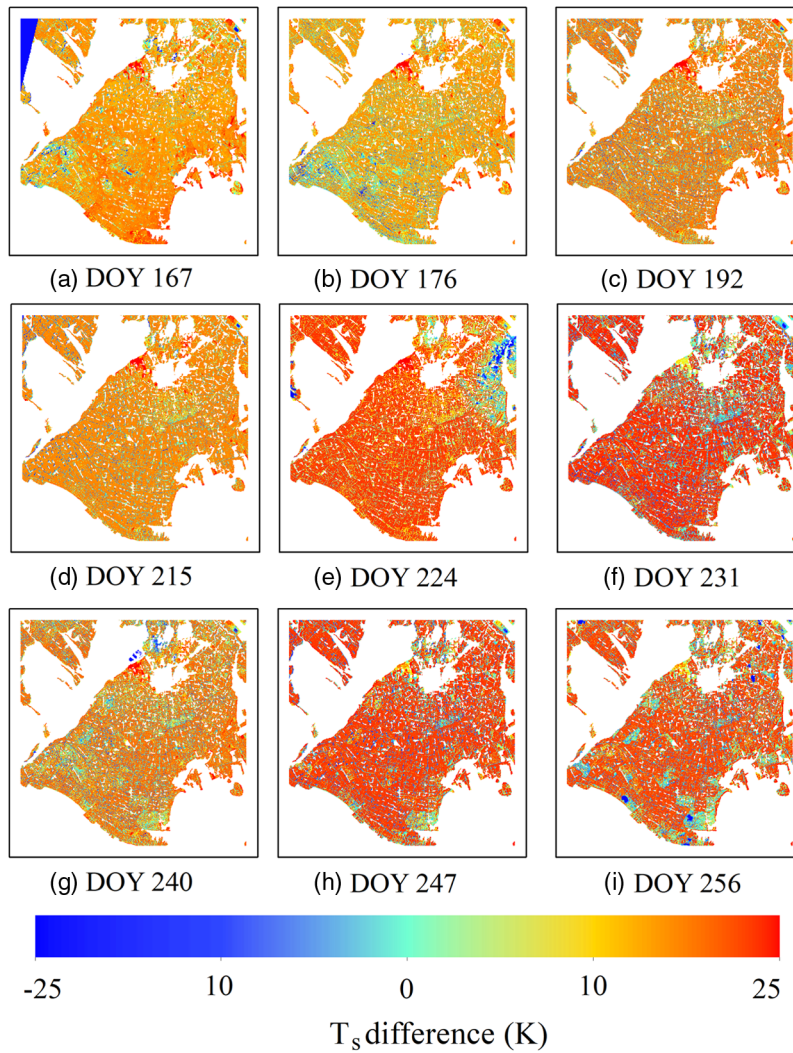


Fig. 6 Soil surface temperature difference estimated using the TSEB- T_R and TSEB-PT methods.

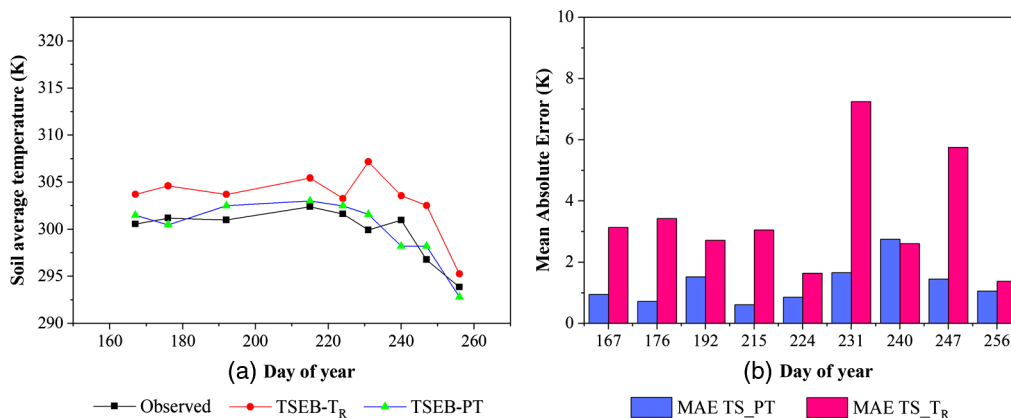


Fig. 7 (a) Average soil temperature values using the TSEB-PT and TSEB- T_R methods compared to those observed on select days. (b) MAE between the observed and estimated values.

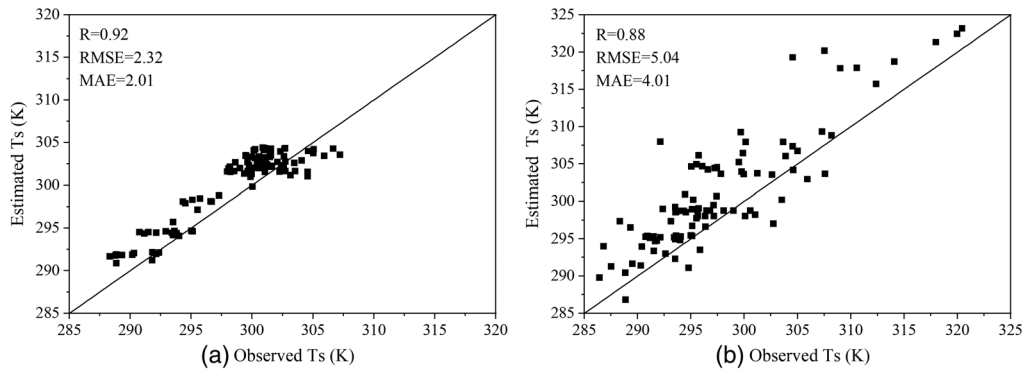


Fig. 8 Comparison of the estimated and observed surface temperatures using (a) the TSEB-PT and (b) TSEB- T_R methods in irrigated cropland. The 1:1 line represents perfect agreement with the observations.

stages of crop growth. Using the TSEB- T_R method, the estimated value of R_n is larger than the observed value, although the difference is not obvious. The discrepancy between the estimated and observed R_n values is smaller using the TSEB- T_R method than the TSEB-PT method. For the TSEB-PT method, the largest discrepancy between the estimated and observed average values occurs on DOY 215, and the difference between them is 61 W m^{-2} . Overall, the difference of the results among the estimated average value and the observed average value is slight.

The range of the observed and estimated values of G is from 80 to 200 W m^{-2} [Fig. 9(b)]. Compared with the observed average value, the estimated value of G is larger when using the TSEB- T_R method. Using the TSEB-PT method, the difference between the estimated and observed values of average G is smaller than that of the TSEB- T_R method. The difference between the observed and estimated average G values is largest in the middle and late stages

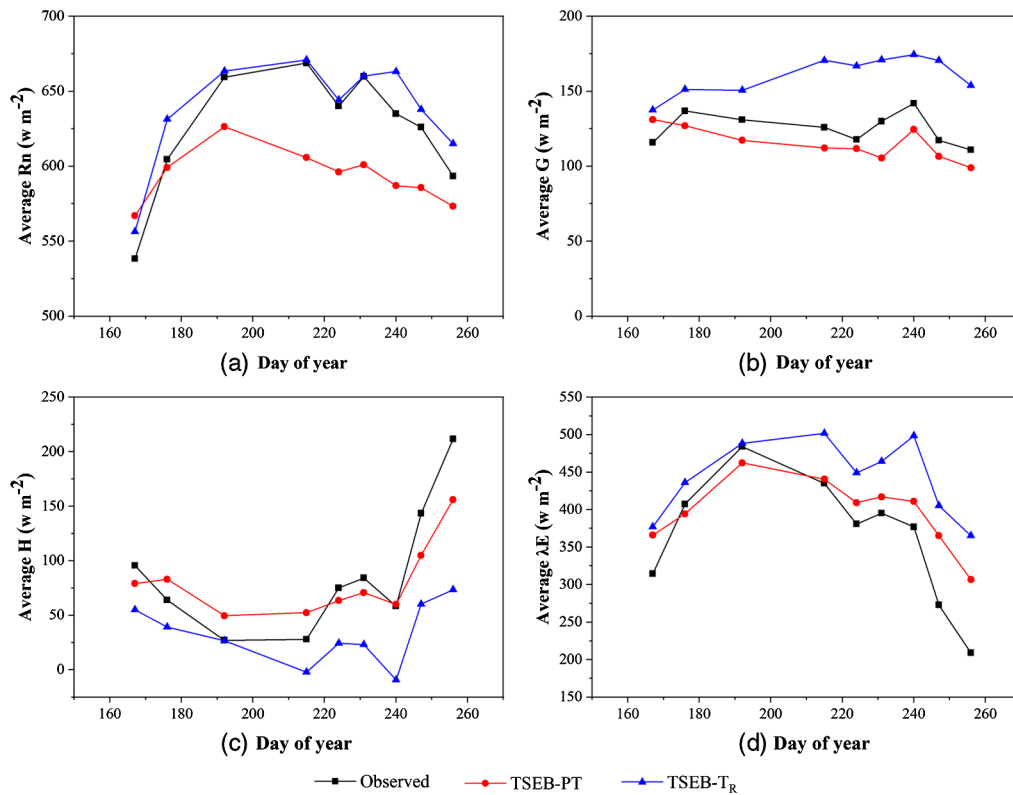


Fig. 9 Comparison of the average estimated net radiation and soil surface heat fluxes using the TSEB- T_R and TSEB-PT methods on select days in an oasis. (a) R_n , (b) G , (c) H , and (d) λE .

of crop growth, which is mainly because G is a function of R_n and can be approximated as a linear relationship. Although the estimated average value is higher than the observed average value, it will not adversely affect the results of estimating λE .

The average estimated H is greater using the TSEB-PT method than using the TSEB- T_R method [Fig. 9(c)]. Compared with the observed values, H estimated via the TSEB-PT method is overestimated in the early stage of crop growth but underestimated in the middle and late stages. As a result, the TSEB- T_R method underestimates the entire crop growth season. Furthermore, the observed value of H is larger than the estimated value from DOY 240 to 256, especially on DOY 256, where the observed average H is 211 W m^{-2} , and the estimated values for the TSEB-PT and TSEB- T_R methods are 156 and 73 W m^{-2} , respectively.

The average values of λE is 200 to 600 W m^{-2} [Fig. 9(d)]. The observed and estimated λE increases from DOY 167 to DOY 192 and then decreases until DOY 256. The average λE estimated via the TSEB-PT method and TSEB- T_R method is larger than the observed value almost throughout the crop growing season. The largest difference occurs from DOY 192 to DOY 256. Moreover, λE estimated using the TSEB-PT method underestimates λE on DOY 176 and DOY 192 and overestimates λE at other times. The time trend shows that the estimated results from the TSEB-PT method are in good agreement with the observed values, with results that are better than the TSEB- T_R method. The reason for the decrease in λE in the later stage of crop growth is that with the beginning of leaf senescence and withering, the transpiration of vegetation tends to stop, the water content of farmland decreases, and the evaporation of surface decreases, resulting in low λE values.

Previous studies have examined the sources of flux measurements in depth in this study area. The results have shown that the main contribution source area of EC measurements per month is within 180 m radius of the Yingke (YK, $100^{\circ}24'37''\text{E}$, $38^{\circ}02'40''\text{N}$) observation point at an 80% contribution level, and the contribution rate increases to its maximum value at ~ 30 m from the observation point.¹² The main wind direction in July is from the north and west. Therefore, these two directions contribute at this time. At this time, the main source areas of EC are wheat and maize underlying surfaces. The main source area for the LAS (with a path length of 2390 m) stretches along a region that is ~ 2000 m long and 700 m wide.²⁸

Based on the energy balance principle, $H + \lambda E$ (turbulent energy fluxes) near the surface should be equal to $R_n - G$ (the available energy). The ratio of the turbulent energy fluxes to the available energy (energy balance ratio, EBR) should be equal to 1.0, where $\text{EBR} = (H + \lambda E)/(R_n - G)$. However, due to the existence of systematic errors, the EBR ranges from 0.7 to 0.9.⁵⁴ In this paper, average values of the observations from all sites are used to calculate the EBR. The results show that the EBR ranges from 0.73 to 0.98, with an average value of 0.88, which is roughly the same as that of Wilson et al.⁵ In other research areas, when only EC data from 06:00 to 18:00 are considered, EBR is about 0.78.⁵⁵ This result indicates that the energy closure reflected by the observed data at different sites is consistent. However, comparing the results obtained by the TSEB-PT and TSEB- T_R methods, EBR is ~ 1.0 . Therefore, the energy closure is very good, and land surface energy balance is balanced.

The reliability of the TSEB model-derived net surface radiation and surface heat fluxes is assessed using two different methods. Scatter plots show dispersion for both the TSEB-PT and TSEB- T_R methods (Fig. 10). A statistical comparison of the model output and observations is shown in Table 1 to demonstrate accuracy and consistency. Based on these results, there are some differences between the TSEB-PT and TSEB- T_R methods.

R_n is underestimated by the TSEB-PT method, whereas using the TSEB- T_R method R_n is overestimated. However, no significant difference is found in these estimates using the different methods. Based on the MAE and RMSE of R_n , there is little difference between the RMSE and MAE of the two methods, and the difference in MAPE is not obvious (5.97% versus 2.42%) (Table 1). The RMSE% value has little difference (2.62% versus 4.12%). The consistency between R_n estimated using the TSEB- T_R method and the observed values is poor ($R = 0.72$) [Fig. 10(a)]. G has a similar RMSE and MAE for the TSEB- T_R and TSEB-PT methods (Table 1). A comparison of the estimated and observed values of G shows that most of the points are located above the 1:1 line for the TSEB- T_R method and TSEB-PT method. These results indicate a tendency for the TSEB- T_R method to overestimate G and the TSEB-PT method to underestimate G [Fig. 10(b)]. When G is less than 60 W m^{-2} , the point is close to 1:1 line,

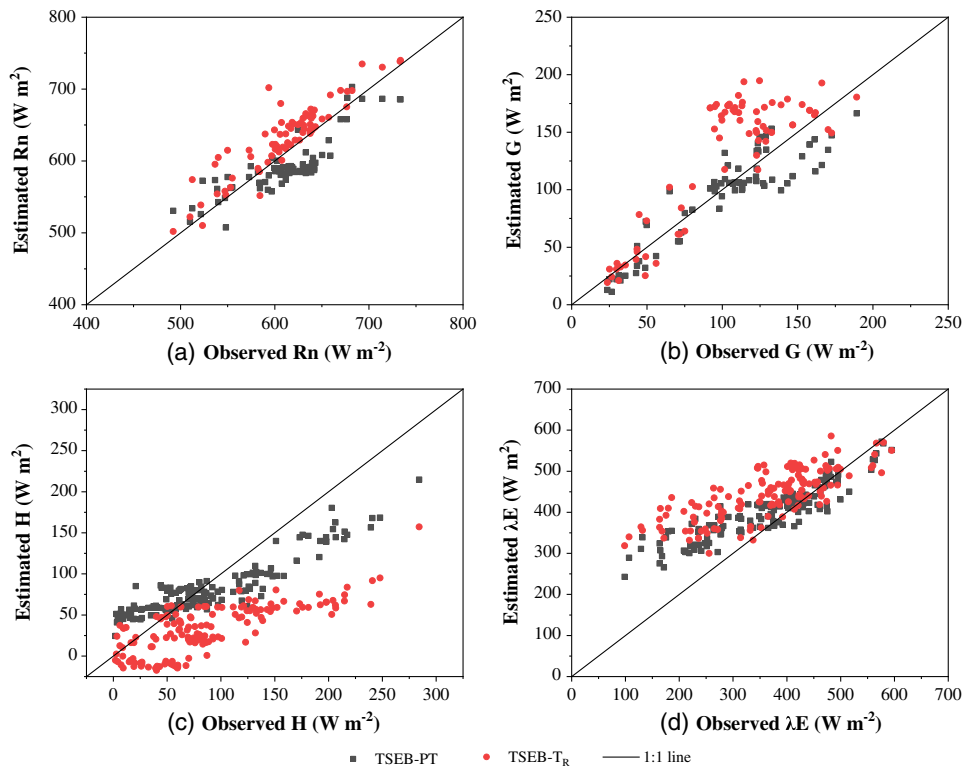


Fig. 10 TSEB model results using the TSEB-PT and TSEB- T_R methods compared to the observed values from the HiWATER measurements for (a) R_n , (b) G , (c) H , and (d) λE . The 1:1 line represents perfect agreement with the observations.

whereas when G is greater than 60 W m^{-2} , the estimated value of the TSEB-PT method is near the 1:1 line but the estimated value of the TSEB- T_R method is far from the 1:1 line, which increases the scatter of points. The correlation between estimated and observed values is good, 0.92 and 0.86, respectively.

Most of the values of H range from 0 to 200 W m^{-2} [Fig. 10(c)]. Comparisons of the observed values and estimated values of the sites show that there are obvious differences between the TSEB-PT and TSEB- T_R methods. For the TSEB- T_R method, H is underestimated, and there is significantly larger scatter. However, using the TSEB-PT method, in the early stage

Table 1 Statistical results of the estimated land surface net radiation and surface heat fluxes compared to the observations using the TSEB-PT and TSEB- T_R methods. See Fig. 10 for scatter plots.

| | TSEB-PT | | | | TSEB- T_R | | | |
|-------------------|---------|--------|-------|-------------|-------------|--------|-------|-------------|
| | R_n | G | H | λE | R_n | G | H | λE |
| Observed average | 625.04 | 125.23 | 87.48 | 364.01 | 625.04 | 125.23 | 87.48 | 364.01 |
| Estimated average | 593.51 | 115.02 | 81.28 | 399.26 | 634.49 | 160.73 | 32.99 | 445.35 |
| RMSE | 16.39 | 9.99 | 22.51 | 46.75 | 25.79 | 10.71 | 61.54 | 76.49 |
| % RMSE | 2.62 | 7.97 | 25.73 | 12.84 | 4.12 | 8.55 | 70.34 | 21.01 |
| MAE | 13.83 | 7.42 | 14.78 | 34.45 | 19.54 | 8.6 | 40.38 | 55.42 |
| MAPE | 5.97 | 10.84 | 32.83 | 15.06 | 2.42 | 28.91 | 62.14 | 27.14 |
| R | 0.9 | 0.92 | 0.98 | 0.95 | 0.72 | 0.86 | 0.81 | 0.75 |

of crop growth, H is overestimated, but underestimated H in the later stage of crop growth. Nevertheless, the observed values agree well with the estimated values, and the points are near of the 1:1 line with less scatter. The statistical results of estimation and observation H show that the TSEB-PT method has good correlation ($R = 0.98$), RMSE and MAE are 22.51 and 14.78 W m^{-2} , respectively, and MAPE is 32.83%. Compared with the TSEB-PT method, the MAPE is large (62.14%) and there is low correlation ($R = 0.81$) when using the TSEB- T_R method (see Table 1).

Under the studied arid and semiarid conditions, the TSEB model solves the problem of turbulent flux distribution between the soil and canopy. Although no measurements of T_c are available for a proper evaluation of this partitioning using the TSEB- T_R and TSEB-PT methods. From an energy balance perspective, λE can be estimated as the residual of R_n , H , and G . Using the TSEB- T_R method, the underestimation of H will cause an overestimation of λE . The TSEB- T_R method results in greater scatter about the 1:1 line for λE , with greater RMSE and MAE values than the TSEB-PT method. The RMSE accuracy increases by 38.8%, and the MAE accuracy increases by 37.9% when applying the TSEB-PT method [Fig. 10(d) and Table 1]. The results show that the estimated values of the TSEB-PT method are in good agreement with the observed value.

4 Discussion

The validation of LST inversion via ground observation has been the primary method.⁵⁶ We validated ASTER LST with 111 point-based LST estimates. The statistical results showed that the MAE and RMSE are 1.37 and 1.6 K (Fig. 4), respectively. The correlation coefficient between the estimated value and the observed value is 0.96. The correlation between the estimated values and observed values is very good, and the accuracy is high; thus, the ASTER LST products is believable. The dataset provides reliable input data for component temperature decomposition and remote sensing estimation of surface net radiation and heat fluxes.

Previous authors have also studied the temperature decomposition of components in this study area,⁴² but no comparative study has been made on the application of other methods in this area. We found that the TSEB-PT method is more suitable for component temperature decomposition. The error between the observed and estimated values is relatively small, and the precision is high. However, when using the TSEB- T_R method for temperature decomposition, the change in vegetation coverage should be considered.¹¹ For the peak LAI, the vegetation coverage is close to 1.0, the estimated soil surface temperature tends to infinity, and T_s is overestimated. In general, the average T_s estimated by the two methods is larger than the observed average T_s , which may also be the result of the observed T_s representing shaded areas in some farmland regions. Although the two methods overestimate T_s , the relative error for the TSEB-PT method is low. The TSEB-PT method provides a method to improve the temperature decomposition accuracy of components similar to that found by Colaizzi et al.,⁵⁷ who used the TSEB- T_c - T_s method to perform temperature decomposition.

The terrain in the study area is relatively flat; therefore, we did not consider the effect of terrain on the R_n calculations. Using the TSEB-PT method, R is 0.9 in this study; however, other studies have used MODIS data⁵⁸ to estimate annual and instantaneous net radiation in this region, where the affecting factors considered included weather conditions, solar zenith angle, volumetric soil moisture, season, and NDVI, and a higher correlation coefficient ($R = 0.94$) was found than the value obtained in this study. Therefore, in the case of more verification points and long time series, the accuracy of R_n will be improved. The vegetation in the study area is mainly maize, and natural vegetation is scarce; in this case, the RMSE and MAE (RMSE = 16.39 W m^{-2} and MAE = 13.83 W m^{-2}) in this paper are less than those reported by Colaizzi et al.,²⁰ where the results included night-time data, and the RMSE and MAE were 30 and 23 W m^{-2} , respectively. Using the TSEB-PT method, the MAE is less than the MAE reported by Kustas et al.,⁵⁹ who used the TSEB- T_R method and showed that the surface was covered with grass and the MAE was 15 W m^{-2} .

Although the model estimation of the G is reasonable. A difference is found between the observed and estimated average G values from the two methods. Significant differences appear

most in crop growing seasons. Early in the season, the canopy coverage is sparse. The net short-wave irradiance to the soil increases by up to 80% of the global shortwave irradiance, resulting in a sharp increase in R_{ns} ; therefore, the value of G increases. Comparing estimated versus observed G [Fig. 10(b)] revealed more scatter in G estimates using the TSEB- T_R method compared to the version using the TSEB-PT method. This is attributed to the parameterization of G to a constant proportion of R_n . Field observations show that G/R_n can range from 0.05 to 0.50.⁶⁰ Overestimation of R_n will inevitably lead to overestimation of G . The results based on the TSEB-PT method are better; the RMSE and MAE of G are similar to those reported by Colaizzi et al.²⁰ where RMSE = 9.3 W m⁻² and MAE = 6.5 W m⁻². However, the RMSE and MAE results are less in this study than those reported by Norman et al.,¹¹ where the RMSE and MAE were 28 and 35 Wm⁻², respectively.

A previous study showed that H contributed an average of 38% of the total λE for fully irrigated crops during full canopy conditions.⁶¹ In this paper, the temperature decomposition in the middle and late stages of crop growth limits the accuracy of H . In the middle and later stages of crop growth during full canopy cover, there are very small differences between the LST and T_c ; hence, the observed and estimated values of T_s are affected by shadows and illumination, and H is underestimated at the end of crop growth. Similarly, underestimates in H were also found in agricultural areas by Colaizzi et al.⁵⁷ Therefore, the method of component temperature decomposition needs to be improved from the middle stage of crop growth to the harvest season. In our study, the RMSE and MAE of H estimated using the TSEB-PT method are 22.51 and 14.78 Wm⁻², respectively, which are less than the results of field experiments estimated by Norman et al.,¹¹ where the RMSE and MAE were 37 and 30 Wm⁻², respectively.

Using the TSEB-PT method, the unrealistic increase in T_s can be limited when f_c is close to 1.0. Under the influence of f_c , using the TSEB- T_R method, the λE error is larger during the middle and later stages of crop growth. The λE values in this study is more scattered for the TSEB- T_R method than the TSEB-PT method. Using the TSEB methods, the results show that the RMSE in λE (RMSE = 46.75 and 76.49 W m⁻², respectively) is lower for farmland, although these results are better than the RMSE of grassland (RMSE = 84 W m⁻²),¹⁷ which indicates that the estimation of λE is different for different underlying surfaces. The soil water stress factors help regulate λE_s under soil drought conditions,⁴² which improves the estimation accuracy of λE (MAE = 34.45 W m⁻²). However, without considering water stress factors, using the TSEB- T_R method to estimate λE results in a higher MAE (MAE = 55.42 W m⁻²), which is close to those estimated under natural semiarid conditions with high vapor pressure deficit and low LAI.²⁷

Because the TSEB model estimated λE as a residual of the energy balance equation, biases from H , R_n , and G might accumulate in the λE estimates and higher nonsystematic errors could be expected.⁶² This averages that the estimation errors of R_n , H , and G strongly influence λE prediction. The TSEB- T_R method overestimates λE in the early and middle stages of crop growth, whereas the TSEB-PT method estimates λE with smaller errors. In the later stage of crop growth, the canopy contains more nontranspiration elements, which may lead to deviations in T_c and T_R ,²⁰ resulting in an underestimation of H [Fig. 9(c)] and overestimation of λE [Fig. 9(d)]. Therefore, the uncertainty in the λE estimation and the error in the R_n and H estimation can explain the discreteness of the λE points in Fig. 10(d). The more discrete the points are, the higher the error. Although the two methods provide a high correlation (R of 0.95 and 0.75), the MAPE for the TSEB-PT method is less than for the TSEB- T_R method (15.06% versus 27.14%).

5 Conclusions

In this paper, two different methods of component temperature decomposition are compared to determine the most suitable method in arid and semiarid areas. Although the results of the two model versions are similar, T_s is overestimated. However, our analysis shows significant differences between the methods at our study area, and the agreement between the estimated and observed T_s is better using the TSEB-PT method than using the TSEB- T_R method; the precision is also higher.

We compared the results of the simulated surface heat flux based on the TSEB model driven by T_s and T_c in arid and semiarid regions. Choosing the most accurate surface heat flux method is the primary focus. To conclude, our analysis shows that the TSEB-PT method can be applied operationally and produces reliable estimates of G , H , and λE in both arid and semiarid regions. Compared to the TSEB- T_R method, the TSEB-PT method provides better estimates of the surface latent heat flux, and the RMSE's effective accuracy is improved by 38.8% in arid and semiarid regions. The TSEB-PT method is a good choice to retrieve surface temperature information from remote sensing data in semiarid areas. The surface temperature can then be decomposed into separate soil and vegetation components, which are then used to estimate the surface heat flux, providing viable results.

Acknowledgments

The author would like to acknowledge the ASTER data provided by the Scientific Data Center for Dry and Cold Areas.³⁴ We also thank the Heihe Watershed Allied Telemetry Experimental Research team for providing observation data downloaded that were used in this study.³⁴ We are thankful to the anonymous reviewers for their constructive comments and suggestions. This has greatly helped raise the quality of paper. The authors have no conflicts of interest to declare.

References

1. G. B. Senay, S. Bohms, and J. P. Verdin, *Remote Sensing of Evapotranspiration for Operational Drought Monitoring using Principles of Water and Energy Balance*, CRC Press, Taylor & Francis Group (2012).
2. G. F. Zhu et al., "Simultaneously assimilating multivariate data sets into the two-source evapotranspiration model by Bayesian approach: application to spring maize in an arid region of Northwestern China," *Geosci. Model Dev.* **7**(4), 1467–1482 (2014).
3. J. A. Tolk et al., "Role of transpiration suppression by evaporation of intercepted water in improving irrigation efficiency," *Irrigation Sci.* **16**(2), 89–95 (1995).
4. A. J. Dyer, "Measurements of evaporation and heat transfer in the lower atmosphere by an automatic eddy-correlation technique," *Q. J. R. Meteorol. Soc.* **89**(382), 556–557 (1963).
5. K. Wilson et al., "Energy balance closure at FLUXNET sites," *Agric. For. Meteorol.* **113**(1–4), 223–243 (2002).
6. T. A. Howell, A. D. Schneider, and M. E. Jensen, "History of lysimeter design and use for evapotranspiration measurements," in *Lysimeters for Evapotranspiration and Environmental Measurements*, R. G. Allen et al., Eds., ASCE, Reston, pp. 1–9 (1991).
7. P. A. Solognac et al., "Uncertainty analysis of computational methods for deriving sensible heat flux values from scintillometer measurements," *Atmos. Meas. Tech.* **2**(2), 741–753 (2009).
8. W. G. M. Bastiaanssen et al., "A remote sensing surface energy balance algorithm for land (SEBAL) - 1. Formulation," *J. Hydrol.* **212**(1–4), 198–212 (1998).
9. W. G. M. Bastiaanssen et al., "A remote sensing surface energy balance algorithm for land (SEBAL) - 2. Validation," *J. Hydrol.* **212**(1–4), 213–229 (1998).
10. Z. Su, "The surface energy balance system (SEBS) for estimation of turbulent heat fluxes," *Hydrol. Earth Syst. Sci.* **6**(1), 85–100 (2002).
11. J. M. Norman, W. P. Kustas, and K. S. Humes, "Source approach for estimating soil and vegetation energy fluxes in observations of directional radiometric surface-temperature," *Agric. For. Meteorol.* **77**(3–4), 263–293 (1995).
12. W. P. Kustas et al., "Single- and dual-source modeling of surface energy fluxes with radiometric surface temperature," *J. Appl. Meteorol.* **35**(1), 110–121 (1996).
13. X. Zhan, W. P. Kustas, and K. S. Humes, "An intercomparison study on models of sensible heat flux over partial canopy surfaces with remotely sensed surface temperature," *Remote Sens. Environ.* **58**(3), 242–256 (1996).
14. W. J. Timmermans et al., "An intercomparison of the surface energy balance algorithm for land (SEBAL) and the two-source energy balance (TSEB) modeling schemes," *Remote Sens. Environ.* **108**(4), 369–384 (2007).

15. W. P. Kustas and J. M. Norman, "Evaluation of soil and vegetation heat flux predictions using a simple two-source model with radiometric temperatures for partial canopy cover," *Agric. For. Meteorol.* **94**(1), 13–29 (1999).
16. M. C. Anderson et al., "A thermal-based remote sensing technique for routine mapping of land-surface carbon, water and energy fluxes from field to regional scales," *Remote Sens. Environ.* **112**(12), 4227–4241 (2008).
17. L. Morillas et al., "Using radiometric surface temperature for surface energy flux estimation in Mediterranean drylands from a two-source perspective," *Remote Sens. Environ.* **136**, 234–246 (2013).
18. K. Mallick et al., "Latent heat flux estimation in clear sky days over Indian agroecosystems using noontime satellite remote sensing data," *Agric. For. Meteorol.* **149**(10), 1646–1665 (2009).
19. G. B. Senay et al., "A coupled remote sensing and simplified surface energy balance approach to estimate actual evapotranspiration from irrigated fields," *Sensors-Basel* **7**(6), 979–1000 (2007).
20. P. D. Colaizzi et al., "Two-source energy balance model estimates of evapotranspiration using component and composite surface temperatures," *Adv. Water Resour.* **50**, 134–151 (2012).
21. W. J. Shuttleworth and J. S. Wallace, "Evaporation from sparse crops: an energy combination theory," *Q. J. R. Meteorol. Soc.* **111**(469), 839–855 (1985).
22. J. S. Wallace, "Evaporation and radiation interception by neighbouring plants," *Q. J. R. Meteorol. Soc.* **123**(543), 1885–1905 (1997).
23. P. Kabat, A. J. Dolman, and J. A. Elbers, "Evaporation, sensible heat and canopy conductance of fallow savannah and patterned woodland in the Sahel," *J. Hydrol.* **189**(1–4), 494–515 (1997).
24. M. C. Anderson et al., "A two-source time-integrated model for estimating surface fluxes using thermal infrared remote sensing," *Remote Sens. Environ.* **60**(2), 195–216 (1997).
25. W. Kustas and M. Anderson, "Advances in thermal infrared remote sensing for land surface modeling," *Agric. For. Meteorol.* **149**(12), 2071–2081 (2009).
26. C. H. B. Priestley and R. J. Taylor, "On the assessment of surface heat flux and evaporation using large-scale parameters," *Mon. Weather Rev.* **100**(2), 81–92 (1972).
27. N. Agam et al., "Application of the Priestley–Taylor approach in a two-source surface energy balance model," *J. Hydrol.* **11**(1), 185–198 (2010).
28. S. M. Liu et al., "A comparison of eddy-covariance and large aperture scintillometer measurements with respect to the energy balance closure problem," *Hydrol. Earth Syst. Sci.* **15**(4), 1291–1306 (2011).
29. A. Gillespie et al., "A temperature and emissivity separation algorithm for advanced spaceborne thermal emission and reflection radiometer (ASTER) images," *IEEE Trans. Geosci. Remote Sens.* **36**(4), 1113–1126 (1998).
30. H. Tonooka, "Accurate atmospheric correction of ASTER thermal infrared imagery using the WVS method," *IEEE Trans. Geosci. Remote Sens.* **43**(12), 2778–2792 (2005).
31. H. Li, "HiWATER: ASTER LST and LSE dataset in 2012 in the middle reaches of the Heihe River Basin," 2012 <http://westdc.westgis.ac.cn/data/43932103-65cd-4b25-a750-8936913efafe>.
32. Y. Sawabe et al., "Temperature and emissivity separation for multi-band radiometer and validation of the ASTER TES algorithm," *J. Remote Sens. Soc. Jpn.* **23**(4), 364–375 (2009).
33. X. Li et al., "Heihe watershed allied telemetry experimental research (HiWATER): scientific objectives and experimental design," *Bull. Am. Meteorol. Soc.* **94**(8), 1145–1160 (2013).
34. S. M. Liu et al., "The Heihe Integrated Observatory Network: a basin-scale land surface processes observatory in China," *Vadose Zone J.* **17**(1) (2018).
35. H. P. Schmid, "Experimental design for flux measurements: matching scales of observations and fluxes," *Agric. For. Meteorol.* **87**(2–3), 179–200 (1997).
36. B. Z. Chen et al., "Characterizing spatial representativeness of flux tower eddy-covariance measurements across the Canadian carbon program network using remote sensing and footprint analysis," *Remote Sens. Environ.* **124**, 742–755 (2012).

37. A. Were et al., "Ventilation of subterranean CO₂ and Eddy covariance incongruities over carbonate ecosystems," *Biogeosciences* **7**(3), 859–867 (2010).
38. H. P. Schmid, "Footprint modeling for vegetation atmosphere exchange studies: a review and perspective," *Agric. For. Meteorol.* **113**(1–4), 159–183 (2002).
39. R. Kormann and F. X. Meixner, "An analytical footprint model for non-neutral stratification," *Boundary Layer Meteorol.* **99**(2), 207–224 (2001).
40. K. Yang and J. Wang, "A temperature prediction-correction method for estimating surface soil heat flux from soil temperature and moisture data," *Sci. China Ser.* **51**(5), 721–729 (2008).
41. J. A. Santanello and M. A. Friedl, "Diurnal covariation in soil heat flux and net radiation," *J. Appl. Meteorol.* **42**(6), 851–862 (2003).
42. L. S. Song et al., "Applications of a thermal-based two-source energy balance model using Priestley–Taylor approach for surface temperature partitioning under advective conditions," *J. Hydrol.* **540**, 574–587 (2016).
43. W. P. Kustas et al., "Revisiting the paper 'Using radiometric surface temperature for surface energy flux estimation in Mediterranean drylands from a two-source perspective'," *Remote Sens. Environ.* **184**, 645–653 (2016).
44. W. Brutsaert, *Evaporation into the Atmosphere: Theory, History and Applications*, D. Reidel Publishing Company, Dordrecht, Holland (1982).
45. S. A. O'Shaughnessy and S. R. Evett, "Developing wireless sensor networks for monitoring crop canopy temperature using a moving sprinkler system as a platform," *Appl. Eng. Agric.* **26**(2), 331–341 (2010).
46. R. Guzinski et al., "Using a thermal-based two source energy balance model with time-differencing to estimate surface energy fluxes with day-night MODIS observations," *Hydrol. Earth Syst. Sci.* **17**(7), 2809–2825 (2013).
47. J. B. Fisher, K. P. Tu, and D. D. Baldocchi, "Global estimates of the land-atmosphere water flux based on monthly AVHRR and ISLSCP-II data, validated at 16 FLUXNET sites," *Remote Sens. Environ.* **112**(3), 901–919 (2008).
48. M. Gebremichael and A. P. Barros, "Evaluation of MODIS gross primary productivity (GPP) in tropical monsoon regions," *Remote Sens. Environ.* **100**(2), 150–166 (2006).
49. E. Valor and V. Caselles, "Mapping land surface emissivity from NDVI: application to European, African, and South American areas," *Remote Sens. Environ.* **57**(3), 167–184 (1996).
50. D. I. Stannard, "Comparison of Penman–Monteith, Shuttleworth–Wallace, and modified Priestley–Taylor evapotranspiration models for wildland vegetation in semiarid rangeland," *Water Resour. Res.* **29**(5), 1379–1392 (1993).
51. P. D. Colaizzi et al., "Two-source energy balance model to calculate E, T, and ET: comparison of Priestley–Taylor and Penman–Monteith formulations and two time scaling methods," *Trans. ASABE* **57**(2), 479–498 (2014).
52. G. S. Campbell and J. M. Norman, *An Introduction to Environmental Biophysics*, Springer, New York (1998).
53. C. J. Willmott, "Some comments on the evaluation of model performance," *Bull. Am. Meteorol. Soc.* **63**(11), 1309–1313 (1982).
54. E. T. Kanemasu et al., "Surface flux measurements in FIFE: an overview," *J. Geophys. Res. Atmos.* **97**(D17), 18547–18555 (1992).
55. R. L. Tang et al., "Evaluating one- and two-source energy balance models in estimating surface evapotranspiration from landsat-derived surface temperature and field measurements," *Int. J. Remote Sens.* **34**(9–10), 3299–3313 (2013).
56. Z. L. Li et al., "Satellite-derived land surface temperature: current status and perspectives," *Remote Sens. Environ.* **131**, 14–37 (2013).
57. P. D. Colaizzi et al., "Two-source energy balance model: refinements and lysimeter tests in the southern high plains," *Trans. ASABE* **55**(2), 551–562 (2012).
58. G. H. Huang et al., "High resolution surface radiation products for studies of regional energy, hydrologic and ecological processes over Heihe river basin, northwest China," *Agric. For. Meteorol.* **230**, 67–78 (2016).

59. W. P. Kustas et al., "Evaluating the two-source energy balance model using local thermal and surface flux observations in a strongly advective irrigated agricultural area," *Adv. Water Resour.* **50**(6), 120–133 (2012).
60. W. P. Kustas, C. S. T. Daughtry, and P. J. Vanoevelen, "Analytical treatment of the relationships between soil heat-flux net-radiation ratio and vegetation indexes," *Remote Sens. Environ.* **46**(3), 319–330 (1993).
61. J. A. Tolk, S. R. Evett, and T. A. Howell, "Advection influences on evapotranspiration of alfalfa in a semiarid climate," *Agron. J.* **98**(6), 1646–1654 (2006).
62. J. D. Kalma, T. R. McVicar, and M. F. McCabe, "Estimating land surface evaporation: a review of methods using remotely sensed surface temperature data," *Surv. Geophys.* **29**(4–5), 421–469 (2008).

Runke Wang received his master's degree in cartography and geographic information systems from Lanzhou Jiaotong University, Lanzhou, China, in 2007. He is now a PhD student in the Laboratory of Remote Sensing and Geospatial Science, Northwest Institute of Eco-Environment and Resources, Chinese Academy of Sciences (CAS). His research interests include quantitative remote sensing and remote sensing technology in ecosystem applications.

Jian Wang is a professor and deputy director of the Department of the Laboratory of Remote Sensing and Geospatial Science, Northwest Institute of Eco-Environment and Resources, CAS. His research field is remote sensing of snow hydrology and ecosystem services, mainly including snow measurement using satellite remote sensing data, snowmelt runoff modeling, and physical-based modeling of snowmelt runoff at the watershed scale.

Gaofeng Zhu received his PhD in applied mathematics from Lanzhou University, Lanzhou, China, in 2008. He is currently a professor at Lanzhou University. His current research includes ecohydrological data fusion modeling.

Hongyi Li received his PhD in cartography and geographic information systems from the Cold and Arid Regions Environmental and Engineering Research Institute (CAREERI), CAS, Lanzhou, China, in 2009. He is currently an assistant researcher with the CAREERI, CAS. His current research includes snow distribution simulations under complex terrain conditions and the remote sensing retrieval of snow parameters.

Donghang Shao received his master's degree in cartography and geographic information systems in the Laboratory of Remote Sensing and Geospatial Science, Northwest Institute of Eco-Environment and Resources, CAS, in 2017. He is now a PhD student in the School of Resources and Environment, University of Electronic Science and Technology of China, Chengdu, Sichuan Province, China. His research interests include quantitative remote sensing.

Xiaohua Hao received his PhD in cartography and geography information systems from the CAREERI, CAS, Lanzhou, China, in 2009. He is currently an assistant researcher with the CAREERI, CAS. His current research focuses on remote sensing retrievals of snow parameters.